Aeroacoustic investigation of a ducted wind turbine employing bio-inspired airfoil profiles

Mostafa Mozafari, [1] Mahyar Sadeghi Malekabadi, [2] Amirhosein Fardi[3], Christoph Bruecker [4] and Mehran Masdari [5].

[1] Faculty of New Sciences and Technologies, University of Tehran, Tehran, Iran.
[2] Faculty of Aerospace Engineering, Sharif University of Technology, Tehran, Iran.
[3] Faculty of Mechanical Engineering, Lakehead University, Thunder Bay, ON P7B 5E1, Canada.
[4,5] City, University of London, Northampton Square, London, EC1V 0HB, UK.

Correspondence should be addressed to Mehran Masdari; mehran.masdari@city.ac.uk

Abstract

Ducted wind turbines for residential purposes are characterized by a lower diameter with respect to conventional wind turbines for on-shore applications. The noise generated by the rotor plays a significant role in the overall aerodynamic noise. By making modifications to the blade sections of the wind turbine, we can alter the contributions of aeroacoustic noise sources. This study introduces innovative wind turbine blade designs inspired by owl wing characteristics, achieving significant noise reduction without compromising aerodynamic performance. A three-dimensional (3D) scan of an owl wing was first employed to derive a family of airfoils. The airfoils were employed to modify the blade of a referenced wind turbine airfoil section at various positions on the blade span to determine a blade operating more efficiently at the tip-speed ratio of the original one. While maintaining the same aerodynamic performance, the bio-inspired profiles show a more uniform pressure coefficient distribution, considerably decreasing in the noise level. Furthermore, this study makes considerable progress in ducted wind turbine design by obtaining an 8 dB noise reduction and a 12% improvement in sound pressure level. An in-depth aerodynamic examination shows a 6.4% rise in thrust force coefficient and optimized power coefficients, reaching a peak at a Tip Speed Ratio (TSR) of 8, demonstrating improved energy conversion efficiency. The results highlight the dual advantage of the innovative design: significant noise reduction and enhanced aerodynamic efficiency, offering a promising alternative for urban wind generation.

Keywords: Ducted Wind Turbine, Aeroacoustics, Barn Owl, Large Eddy Simulation.

Nomenclatures

AOA	Angle of Attack	C_T	thrust force coefficient
c	Chord of Airfoil	TSR	Tip Speed Ratio
C_l	Lift Coefficient	SPL	Sound Pressure Level
C_d	Drag Coefficient	OASPL	Overall Sound Pressure Level
Cl/Cd	Lift-to-drag ratio	C_{PWR}	Power Coefficient
2D / 3D	Two / Three Dimensional	LES	Large Eddy Simulation
WT	Wind Turbine	FW-H	Ffowcs Williams-Hawkings
DWT	Ducted Wind Turbine	CFD	Computational Fluid Dynamics

Introduction

The effect of rising global warming has shifted the world to clean energy sources; the most efficient source of clean energy is wind energy [1]. The use of such renewable energy has grown rapidly [2], to the point of justifying the usage of wind turbines in profitable locations in urban areas, to reduce the costs of energy delivery to the user. The integration in the urban environment comes at the cost of reducing the rotor sizes of the wind turbine, by adding a duct to increase the incoming flow speed lowering the effect of incoming turbulent fluctuations, and having to respect more stringent aeroacoustic regulations [3].

The reduction of the wind turbine rotor changes the contributions of the aeroacoustic noise sources, since the turbine is now operating at a relatively lower Reynolds number and at a much higher rotational speed than a conventional one. In this respect, the loading and thickness contributions are no longer negligible. The overall aerodynamic noise is a combination of the one produced by the rotor and the one determined by the duct. While a lot of studies have focused on the coupling between the duct or diffuser and the rotor, only a few have proposed the use of specific airfoils for such low Reynolds number and high turbulence applications. Bio-inspired airfoils have been shown to possess particular characteristics to allow birds to fly in very turbulent environments, with an extremely high lift-to-drag ratio, and at the same time do silently [4]. This has inspired the use of such airfoils for drones and small rotor applications. Despite being known for their feather characteristics, owl's wings have an additional characteristic. The high lift-to-drag ratio of the profile, allows the bird to enormously reduce the flying speed to sustain the bird's weight. Combined with the additional serrated leading edge, the velvety surface and the fringes at the trailing edge, the owl's wing performance is the most silent in the animal kingdom in the final phase of attacking the prey [5-7]. From an aerodynamic point of view the combination of the previous factors, seems to also produce a more favorable and thinner boundary layer, which helps in increasing the aerodynamic performance of the wing. Various studies have been performed experimentally [8, 9], numerically [10-12] and in real flight [13] to use the owl wing characteristics.

In the realm of aerodynamics, flow and noise control are pivotal for enhancing the performance and reducing the environmental impact of wind turbines. Two primary methods are employed to achieve these objectives: active and passive flow control techniques. Active methods, such as the use of dielectric barrier discharge plasma actuators demonstrated by Lee et al. [14], actively manipulate the flow field around structures to control separation and reduce drag, thereby influencing noise generation. On the other hand, passive methods involve structural modifications to the body, which passively influence the flow and noise characteristics. An example is the use of grooved surfaces on deflectors to improve the aerodynamic performance of Savonius wind turbines, as explored by Fatahian et al. [15]. This research aligns with passive flow control strategies by adopting a bio-inspired model that leverages the silent flight characteristics of owl wings. The integration of airfoil profiles inspired by the natural wing structure of owls represents a novel approach in the design of ducted wind turbines to passively control flow and reduce noise. Such bio-inspired designs, as evidenced by the comparative analysis of flow control over a circular cylinder with detached flexible and rigid splitter plates by Eydi et al. [16], underscore the potential of nature-inspired solutions in engineering applications. Our study builds upon this foundation, employing passive flow control through bio-mimicry to achieve a harmonious balance between aerodynamic efficiency and noise reduction in wind turbine design. Additionally, Song et al. [17]demonstrated that the bionic edge design strategy can effectively control the turbulent flow field and effectively break down airflow near the trailing edge. This leads to improved thrust and decreased noise levels.

According to the literature review in this study, it was concluded that very few studies focused on isolating the airfoil characteristics and employing them for industrial applications. In a study by Liu et al. [18], a laser scanner was used to scan the owl wing and characterize its geometric characteristics. These characteristics included camber, chord, twist, and thickness distribution. An analysis of flow interactions with surfaces and flow physics surrounding an owl airfoil was conducted by Klan et al. [19]. Bachmann et al. [20] provided a comprehensive characterization of the wings and feathers of barn owls in high spatial resolution. They conclude that barn owls have evolved specialized wings and feathers to reduce flight noise. To investigate the wings at high spatial resolution, they used confocal laser scanning microscopy, surface digitizing, and computed tomography. They found that these birds of prey have huge wings relative to their body mass, which enables slow flights with increased maneuverability. At low speeds, the researchers found that modifications to the wings' surfaces and edges helped stabilize airflow. Geyer et al. [21] conducted a comprehensive study on owl wings. In addition to performing numerical calculations, they conducted laboratory tests on the wings of owls and several other birds. According to their findings, an owl's wings can be 20 decibels quieter than other birds' wings when gliding. This was achieved by exploiting the relatively lower speed at which the owl’s profile was able to operate. Kondo et al. [22] studied the aerodynamic characteristics of an owl-like airfoil at a Reynolds number of 2300. Their results indicate that the deeply concave lower surface of the owl-like airfoil contributes to lift augmentation, and both a round leading edge and a flat upper surface lead to lift enhancement and drag reduction, determined by the presence of a thin laminar separation bubble near the leading edge. Subsequently, the owl-like airfoil has a higher lift-to-drag ratio than the high lift-to-drag Ishii airfoil at low Reynolds number. A new airfoil for the wind turbine blades was designed and used in the wind turbine blades by Tian et al. [23]. Results show that the bio-inspired airfoil inspired by the Long-eared Owl's wing has a superior lift coefficient and stalling performance, and thus can enhance wind turbine blade performance. An owl inspired airfoil without serrations and a Downy wing surface was compared to a NACA airfoil at low Reynolds numbers by Anyoji et al. [24]. According to their results, the owl inspired airfoil has more lift and generally performs better than the base airfoil at low Reynolds numbers. Moslem et al. [25] demonstrated that a bioinspired propeller not only diminishes both harmonic and broadband noise but also achieves a superior noise level compared to the baseline configuration. Aono et al. [26] investigated the aerodynamics of an owl wing-like airfoil for low Reynolds numbers using numerical methods and the LES turbulence model. They compared the simulation results with several conventional airfoils and showed that the owl wing-inspired airfoil has a higher lift-to-drag coefficient than the other airfoils compared. They reported that this increase was due to the creation of a high-pressure area in the suction area of the airfoil due to the curvature of the owl airfoil. Muthuramalingam et al. [27] explored laminar flow control by employing leading-edge serration, demonstrating a postponement in the transition from laminar to turbulent flow. This effect parallels the phenomenon observed in owl flight, contributing to further noise reduction. Despite all the previous results, whether these airfoils can be reliably applied for a rotating blade at low Reynolds number is still under debate. While in fact the aspect ratio is very similar, the loading distribution of a rotating blade is relatively different from the distribution of a bird’s wing in gliding conditions.

In this manuscript, an investigation is made to study how bio-inspired airfoils could be employed to outperform the loading distribution of a rotating blade. The study proceeds by evaluating how the aerodynamic performance would affect the aeroacoustic footprint of the rotor, including loading and thickness noise and discussing the broadband part due to the change in boundary layer characteristics. The manuscript is organized as follows: In section 2 of this research, a family of airfoils is produced through 3D scanning. These airfoils are then utilized in the design of ducted wind turbine blades, as detailed in section 3. The following sections present a comprehensive numerical analysis of cases (benchmark and multi-section blades), along with the results of aerodynamic and aeroacoustic prediction.

Airfoil family generation

To generate a family of bio-inspired airfoils, a taxidermy owl as shown in Figure 1 has been placed in the center of a 3D scanner. Circular targets mark the owl wing to allow for combining multiple fields of view in a unique 3D reconstruction. In this test, the Solutionix C500-Structured Light 3D Scanner has been used, with a final reconstruction accuracy of 0.01 mm. The center points of the wing are relatively less accurate, due to possible errors induced by the presence of the velvet surface and the feathers.

Illustrated below is the barn owl wing alongside its corresponding reverse model (Figure 2). The airfoil sections exhibit varying airfoil shapes and chord lengths. The data fitting procedure involved using MATLAB to employ Polynomial fitting. For both the upper and lower surfaces of the airfoil, an independent polynomial of degree six was selected. Figure 3 provides an illustrative instance featuring the root airfoil, offering a visualization of its equations and the associated fitting curve.

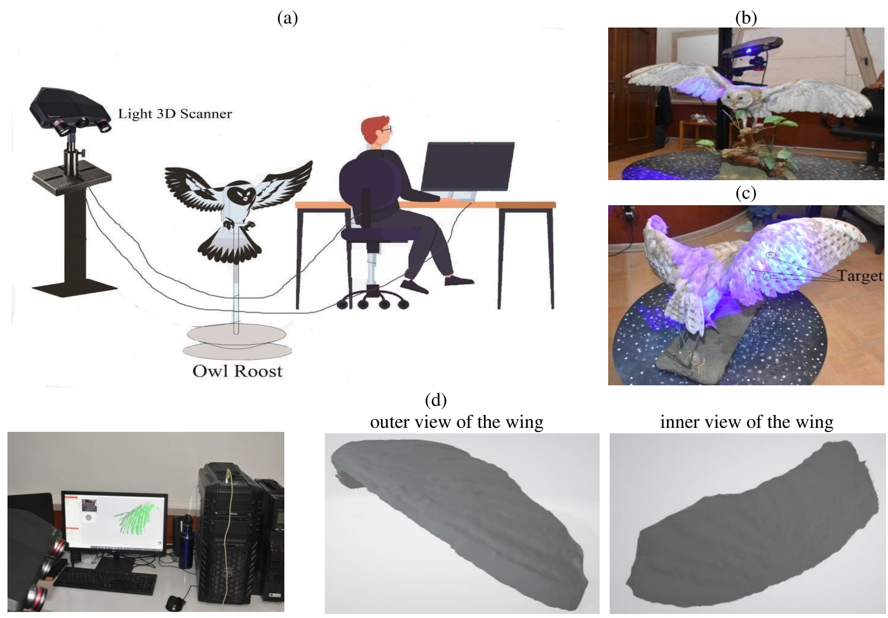

Figure 1: the experimental set-up. (a) A general illustration of the experimental setup. (b) An owl with the camera laser (c) A close view of the laser light sheet with targets on the owl wing (d) 3-D scan output of the owl's wing.

(a) (b)

Figure 2: (a) Barn owl wing, (b) inverted owl wing model.

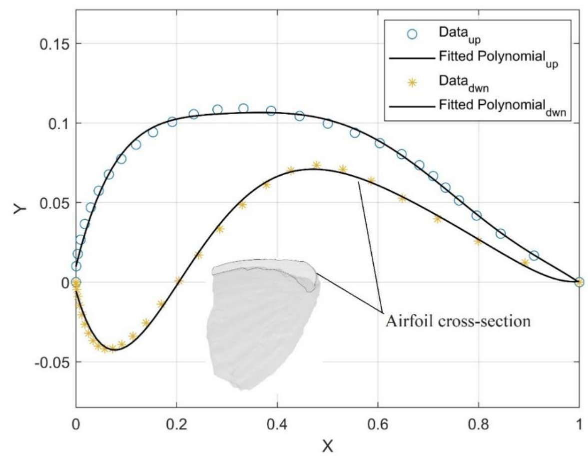

Figure 3: Fitting Results for Airfoil Profile.

The extracted airfoil exhibits a maximum thickness of 12% at x/c=0.11. In the study by Klan et al. [19], these characteristics are documented as 14.77% and 0.15, respectively. It's important to acknowledge a slight variance in the airfoil's overall specifications, potentially stemming from the owl's taxidermy process and water loss from the bird's body. Furthermore, the airfoil features a cusp-type trailing edge, consistent with the research of Ricks et al. [28], which suggests that such a slender trailing edge is associated with reduced noise generation. As indicated, the spatial arrangement of the upper and lower airfoil surfaces has been approximated using a 6th degree polynomial function. This function, denoted as $y_c = ax^6 + bx^5 + cx^4 + dx^3 + ex^2 + fx + g$, has coefficients detailed in Table 1. Here, 'x' represents the positional coordinates along the direction of the airfoil chord.

Table 1: Polynomial Coefficients for Geometric Approximation of Airfoil Surfaces.

Type	a	b	c	d	e	f	g
upper surface	-6.62	23	-30.77	20.1	-6.98	1.266	0.01
lower surface	7.76	-28.33	41.31	-29.72	10.10	-1.1	-0.0056

Blade Design

After scanning the owl's wing, as depicted in Figure 4, a comprehensive numerical analysis was conducted in the vicinity of the owl's wing across a range of frequencies. The simulation was carried out using ANSYS-FLUENT software, employing the LES turbulence model and FW-H acoustic analogy. The domain is subjected to boundary conditions, with velocity inlet and pressure outlet. Additionally, a symmetry condition is applied to surface included the wing root. The computational domain had dimensions of 0.5 * 0.8 * 2 meters, with a mesh count of 0.5 million. Based on sound pressure level measurements conducted by Gruschka et al. [29], it was established that the owl's sound remains inaudible beyond a 3-meter distance for frequencies below 2000 Hz. Consequently, it was decided to incorporate SPL contour tuned to frequencies of 500, 1000, 1600, and 2000 Hz. Moreover, a recurring pattern can be observed across different frequencies in all four cases. Additionally, the following section presents the OASPL curve for the wing sections along the span direction. Upon examination of this curve, it became evident that specific locations along the span of the owl's wing consistently exhibited lower noise levels compared to others. Consequently, these positions were selected as the preferred locations for airfoil extraction. In the selection of these positions, careful consideration was given to choose justifiable points within the range. These positions were identified at 3%, 12.5%, 27%, 44%, and 68% of the owl wing's span, respectively. The reduction in noise during owl flight was attributed to the distinctive characteristics of its airfoil.

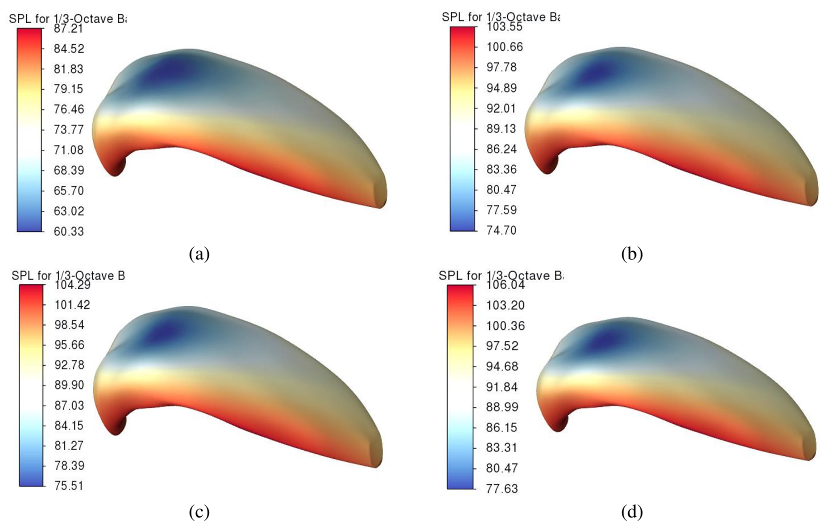

Figure 4: Noise level contours (a) 500 Hz, (b) 1 kHz, (c) 1.6 kHz and (d) 2 kHz.

In light of this discovery, as depicted in Figure 5a, the decision was made to extract and employ these airfoil characteristics from the owl's wing as the preferred airfoil profiles for blade design. The distribution of OASPL shows minimal variations along the owl's wingspan. Interpolation has been utilized to pinpoint cross-sectional data, with selections made at intervals of 7%, 15%, 30%, 50%, and 70% of the blade span. To align with the structural characteristics of the WT, the airfoil for the WT is chosen based on approximately 70% of the actual owl wing (Arm wing). The selected positions of the airfoils are approximately consistent with the minimum locations in the OASPL curve. Consequently, the airfoil of the last section is selected as the tip airfoil for the wind turbine. Wolf and Konrath [30] conducted measurements of the three-dimensional shape of an owl's wing during a flapping cycle. The airfoils derived from the wings of the taxidermy owl examined in this study closely resemble the configuration observed during the gliding phase at a position approximately 5 meters along the right-to-left flight direction. Furthermore, as shown in Figure 5b, these acquired airfoil profiles were utilized to create various sections of the ducted wind turbine. These airfoils were subsequently proportionally scaled and adjusted according to the specifications outlined in Table 2 to align with the design requirements of the desired wind turbine. The ducted wind turbine is designed based on the owl's wing but with some modifications to improve the noise reduction for urban installations.

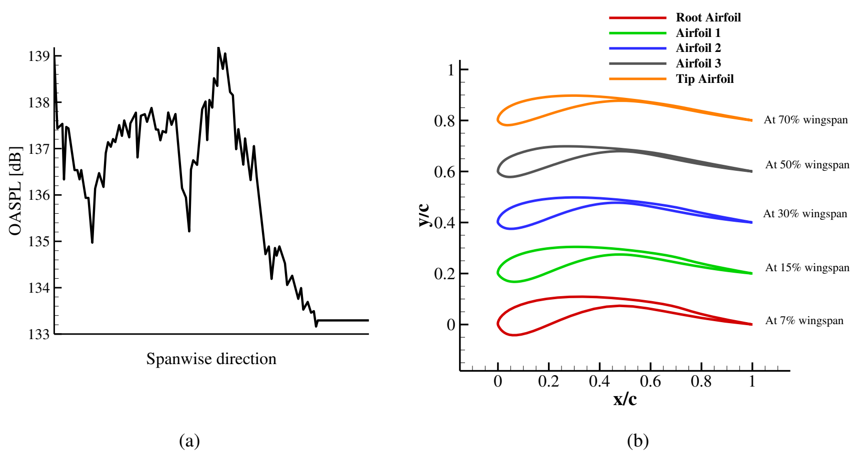

Figure 5: (a) the distribution curve of OASPL in the spanwise direction and illustrating the definition of the position of the selected airfoils, (b) Airfoils section inspired by owl wings.

As depicted in Figure 6, the airfoils for various sections draw inspiration from owl wings in shaping the desired geometry (refer to Table 2). Within the framework of DWT blade design, a consistent airfoil is established within each of the delineated sections. However, to seamlessly interlink these sections, the loft feature is implemented in CAD Software, allowing for adaptable variation of the airfoil along the span. The turbine has a duct length of 1 meter and an internal diameter of 1.6 meters.

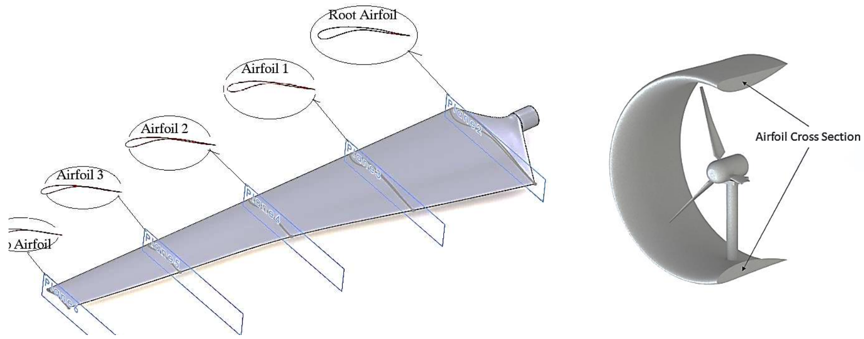

Figure 6: Schematic of the ducted wind turbine and multi-section blade.

Table 2: Design Features of Turbine.

Airfoils	Chord (m)
Root Airfoil	0.16
Airfoil 1	0.12
Airfoil 2	0.08
Airfoil 3	0.06
Tip Airfoil	0.04
Duct Airfoil	1

Cases examined

This research involved two simulations, which are described in brief below. In this simulation, unsteady, compressible conditions are used in conjunction with LES turbulence model and FW-H acoustic analogy.

1. Case 1: (Benchmark Blade- DonQi® wind turbine [31]).
2. Case 2: (Multi-section Blade) Use of airfoils of different sections of the owl wing for blade sections: This case was done to investigate the effect of changing the airfoil and the use of airfoils of different sections of the owl wing in different sections of the blade.

Governing equations

This study utilized computational fluid dynamics with the Large Eddy Simulation (LES) method for fluid flow analysis and the Ffowcs Williams and Hawkings (FW–H) acoustic analogy for acoustic analysis. The governing equations for each method are detailed below.

Fluid dynamics

Turbulent flows are characterized by eddies with a wide range of length and time scales. In the Large Eddy Simulation (LES) method, large eddies are solved directly and small eddies are also modeled. The governing equations employed for LES are obtained by filtering the time-dependent Navier-Stokes equations in either Fourier (wave-number) space or configuration (physical) space. Filtering the Navier-Stokes equations, one obtains [32]:

$$\frac{\partial \rho}{\partial t}+\frac{\partial}{\partial x_i}\left(\rho \overline{u_i}\right)=0 \qquad (1)$$

And

$$\frac{\partial}{\partial t}\left(\rho \overline{u_i}\right)+\frac{\partial}{\partial x_j}\left(\rho \overline{u_i}\,\overline{u_j}\right)=\frac{\partial}{\partial x_j}\left(\mu \frac{\partial \sigma_{ij}}{\partial x_j}\right)-\frac{\partial \overline{p}}{\partial x_i}-\frac{\partial \tau_{ij}}{\partial x_j} \qquad (2)$$

where u, ρ, μ and p are the fluid velocity, density, turbulent viscosity, and static pressure, and i and j are the subscripts with 1 and 2 for the x and y directions. Also, σ_{ij} is the stress tensor due to molecular viscosity and τ_{ij} is the subgrid-scale stress.

Acoustics

Lighthill proposed the theory of the difference between real flow and reference flow and called it analogy. Ffowcs Williams-Hawkings (FW-H) then challenged it and used to give solutions to Lighthill's equation for a medium that includes moving surfaces and convected turbulent flow. In this research, FW-H formulation has been used to model the propagation of sound from a moving source [33, 34].

$$\frac{1}{c_\infty^{\,2}}\frac{\partial^2 p'}{\partial t^2}-\frac{\partial^2 p'}{\partial x_i^{\,2}}=\frac{\partial^2}{\partial x_i \partial x_j}\left\{T_{ij}H(f)\right\}-\frac{\partial}{\partial x_i}\left\{\left[P_{ij}n_j+\rho u_i\left(u_n-v_n\right)\right]\delta(f)\right\} + \frac{\partial}{\partial t}\left\{\left[\rho_\infty v_n+\rho\left(u_n-v_n\right)\right]\delta(f)\right\} \qquad (3)$$

Where u_n and u_i are the fluid velocity in the normal direction of the integration surface and in x_i direction, respectively. v_n and v_i represent the normal velocity of the integration surface and the surface velocity component in x_i direction. $H(f)$ is Heaviside function and $\delta(f)$ is Dirac delta function. p' is sound pressure in the far field ($p'=p-p_\infty$), n_j normal vector pointing to the external area ($f>0$), c_∞ is speed of sound in the far field, P_{ij} is compressive stress tensor and T_{ij} is the Lighthill's stress tensor, given by:

$$T_{ij}=\rho v_i v_j+p_{ij}-\left(\rho-\rho_\infty\right)c_\infty^{\,2}\delta_{ij} \qquad (4)$$

To solve Equation (3), the Green's function must be used to the open area. The complete solution involves the calculation of surface and volume integrals, the first representing monopole, dipole, and partially quadrupole acoustic sources, and the second representing quadrupole sources in the area outside of the source surface. The volume integral becomes negligible when the Mach number value of the flow is small and the source area covers the source area. In Ansys Fluent, choosing a source on a solid surface-like rotor, the volume integrals are neglected, and then the equation takes the following form [35]:

$$p'\left(\vec{x},t\right)=p'_T\left(\vec{x},t\right)+p'_L\left(\vec{x},t\right) \tag{5}$$

In equation (5), t is the observer time, $\vec{x}$ is the receiver position. The subscripts T and L. L refer to the thickness (monopole) and loading (dipole) components, respectively and are given as follows [33, 34]:

$$4\pi p'_T\left(\vec{x},t\right)=\int_{f=0}\left[\frac{\rho_\infty\left(\dot{U}_n+U_{\dot{n}}\right)}{r\left(1-M_r\right)^2}\right]ds+\int_{f=0}\left[\frac{\rho_\infty U_n\left(r\dot{M}_r+c_\infty\left(M_r-M^2\right)\right)}{r^2\left(1-M_r\right)^3}\right]ds \tag{6}$$

$$\begin{aligned}4\pi p'_L\left(\vec{x},t\right)=\frac{1}{c_\infty}\int_{f=0}\left[\frac{\dot{L}_r}{r\left(1-M_r\right)^2}\right]ds+\int_{f=0}\left[\frac{L_r-L_M}{r\left(1-M_r\right)^2}\right]ds\\+\frac{1}{c_\infty}\int_{f=0}\left[\frac{L_r\left\{rM_r+c_\infty\left(\dot{M}_r-M^2\right)\right\}}{r^2\left(1-M_r\right)^3}\right]ds\end{aligned} \tag{17}$$

Where:

$$U_i=v_i+\frac{\rho}{\rho_\infty}\left(u_i-v_i\right)$$
$$L_i=P_{ij}\hat{n}_j+\rho u_i\left(u_n-v_n\right)$$

Where M and r represent the surface velocity vector and the unit radiation vector. The two terms $p'_T\left(\vec{x},t\right)$ and $p'_L\left(\vec{x},t\right)$ in Equation (5) are referred to as thickness and loading terms, respectively.

Numerical solver

The commercial software ANSYS-FLUENT has been used for all simulations carried out in this work. For an accurate calculation of the flow field around the blade, the LES solution was calculated with the Fluent SIMPLE solver. This approach has been proven suitable to describe similar problems in wind turbines. This solver used the finite volume method as a discretization procedure with Bounded Central Differences for momentum and Second Order Central Differences for pressure. A Bounded Second Order Implicit scheme is used for the time marching method in the present work as a temporal discretization scheme with the convergence criteria of 10^{-4}. Since the Mach number at the blades of a wind turbine is always less than 0.2, the air has been modeled as incompressible for reducing the computational costs while maintaining accuracy.

The 3D mesh of the full rotor was carried out first by drawing it in the SpaceClaim software, while the mesh generation was performed using Fluent Meshing. For this problem, a polyhexcore mesh is generated. The computational domain is divided into two parts: the internal rotating field and the external relatively stationary flow field. The interfaces are set to transfer data between the rotational and stationary parts. Coupled problems between the two parts have a significant influence on the accuracy of numerical simulation. In the present study, the sliding mesh model is used to account for the rotation of the blades.

Figure 7 shows the boundary conditions, including velocity inlet and pressure outlet boundaries used to simulate the far field flow. In this case, the velocity of the free stream is 5 m/s, corresponding to the Reynolds number (Re) based on the duct chord length c ($Re=3.4*10^5$). The rotational speed of the wind turbine is 39.84 rad/s. distance from the main inlet boundary to the leading edge of the blade is 10×c and the distance from the leading edge to the main outlet boundary is 20×c.

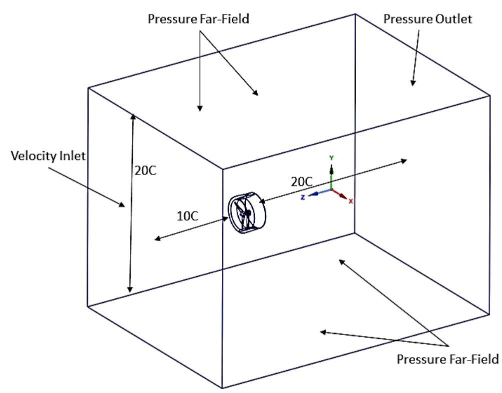

Figure 7: Computational domain used for the LES simulation. The length is indicated in terms of duct chord length c.

According to Figure 8, the computational domain is discretized by about 6 million cells. The fine mesh is used on the whole rotor surface and gradually becomes coarser as the distance from the blades increases. Technique based on the previous results of k-epsilon turbulence model have been used to evaluate the grid resolution in LES method. In this technique, parameter f, has been calculated for the entire computing field by RANS model. The parameter f denotes the ratio of the integral turbulence length scale to the filter width. This can be simplified and expressed as $f = k^{3/2} / (\varepsilon \times (\text{Cell Volume})^{1/3})$, where k represents kinetic energy and ε signifies turbulent dissipation [36]. In most areas, this value is of the order of 5-10, which indicates the good quality of the mesh. Therefore, the grid resolution meets the requirements for the LES calculation.

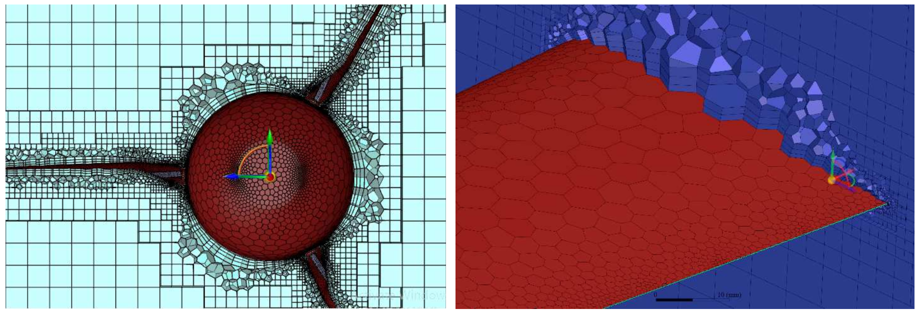

(a) (b)

Figure 8: Schematic view of the computational domain. (a) Front view of DWT and (b) Side view of the blade.

Results and Discussion

Validation

The validation method for this research was conducted with great attention to details. It involved a rigorous comparison between the thrust force coefficient (C_T), which is derived from the pressure coefficient (Cp) along the chord, and the reference data obtained from Ten Hoopen's study described in reference [37]. The main objective was not to precisely reproduce the Cp values at each location on the surface along the chord, but rather to guarantee that the general pattern of Cp distribution closely corresponds to the reference, as illustrated in Figure 9. The key element of our validation process involved comparing the precise values of C_T, with a specific emphasis on the correlation between the thrust ratio in our simulation and the reference of [37].

It is important to note that Ten Hoopen's work lacks detailed information regarding the manufacturing accuracy of the model and the precision of the measuring instruments. This implies that achieving a precise match for local Cp values between the simulated results and the reference data may not be possible. Hence, our validation focused on confirming the pattern of behavior and the distribution curve of pressure.

In the present context, the validation of the simulation, which relies on the Donqi blade results and is supplemented by the experimental findings of Ten Hoopen [37], demonstrates a fundamental similarity in pressure distributions. However, there are slight variations observed in the vicinity of the suction peak region, which may be attributed to assumptions made during the simulation or inherent uncertainties in the experimental data. This validation verifies that the aerodynamic characteristics of the ducted wind turbine (DWT) are accurately represented and simulated, especially when examining how the pressure distributions react to different wake propagation velocities (V_w), which in turn affect the maximum absolute pressures on various sides of the airfoil. Therefore, the duct thrust force coefficient (C_T) has played a crucial role in our work by calculating the grid resolution and assessing the aerodynamic changes in the DWT models. This ensures that our technique closely matches the established experimental standards. Table 3 presents a comparison of various grids against experimental and numerical results. The table indicates that the error for the 6 million grid was kept below 10%, meeting the required accuracy standards. Therefore, the chosen grid number for this study was 6 million. The multi-section blade exhibited a 6.4 % increase in thrust force coefficient compared to the conventional blade.

Table 3: Comparison of the thrust force coefficient.

	Experimental Value [37]	2.7 million numerical value (Benchmark)	LES Error (%)	4.3 million numerical value (Benchmark)	LES Error (%)	6 million numerical value (Benchmark)	LES Error (%)	6 million numerical value (Multi-section)	Difference Value (percentage increase)
thrust force coefficient, C_T	0.689	0.811	17.7	0.773	12.2	0.735	6.7	0.782	6.4

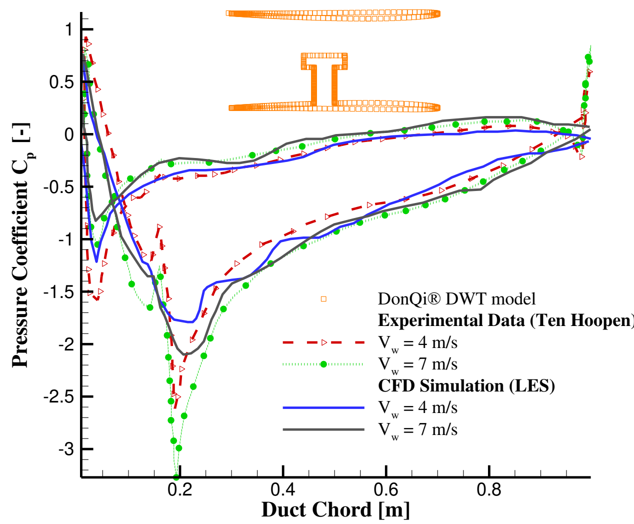

Figure 9: Comparison between numerical and experimental solution of pressure distribution.

To validate the acoustic findings in our present study, we have conducted a comparative analysis of the Power Spectral Density graph of the acoustic pressure, focusing on the blade passing frequency, as illustrated in Figure 10. This evaluation was undertaken at the microphone location set at 90 degrees for the DonQi® DWT model, as examined by Dighe et al, [31]. It's evident that minimal deviations exist for blade passing frequencies below 2, with more pronounced discrepancies emerging at higher frequencies. Overall distribution has similar characteristic which the 2^{nd} harmonic is less pronounced, and the 4^{th} harmonic stronger. Importantly, our LES approach not only captures these variations but also effectively characterizes the transitional trends.

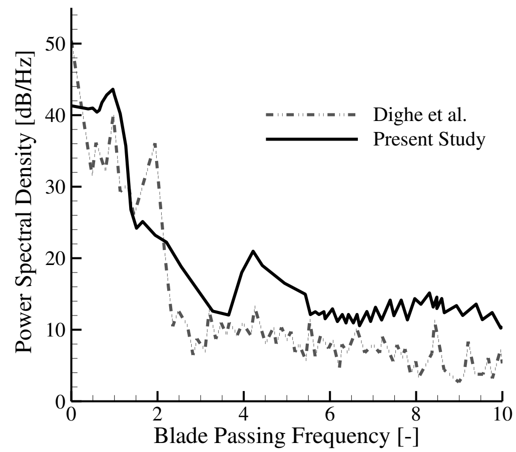

Figure 10: Validating Acoustic Results.

Aerodynamics results

This section focuses on the analysis of the characteristic of the owl airfoil compared to a conventional airfoil in a 2D context used for wind turbine. The evaluation is carried out by analyzing the aerodynamic properties of both types of airfoils, and the results are discussed in this section.

Figure 11 illustrate the pressure contour for the owl and benchmark airfoils at angles of attack of 0 and 6 degrees. The unique shape of the owl airfoil, characterized by a thicker leading edge, higher curvature, and thinner trailing edge, generates a separation bubble. More pronounced in the owl airfoil Compared to a standard reference, leading to a more significant pressure difference and, in turn, increased lift (as depicted in Figure 12).

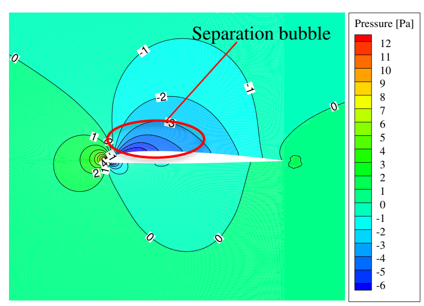

(a) Benchmark airfoil at AOA = 0∘

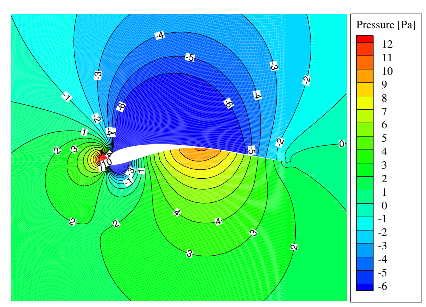

(b) Owl's airfoil at AOA = 0∘

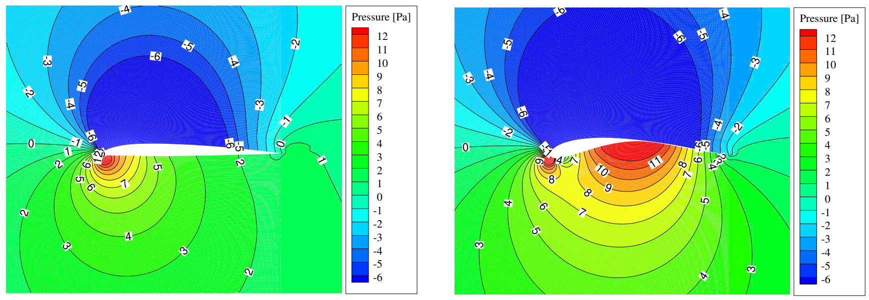

(c) Benchmark airfoil at AOA = 6◦   (d) Owl's airfoil at AOA = 6◦

Figure 11: The pressure contour at different angles of attack.

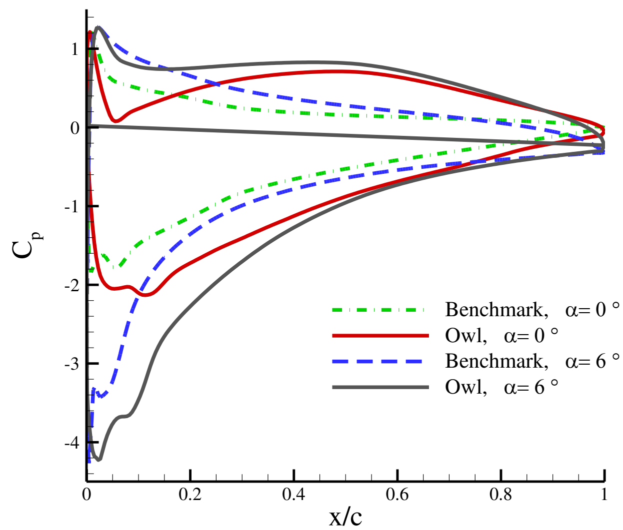

Figure 12: Cp comparison between Owl and benchmark airfoils for AOA= 0◦ and AOA= 6◦.

In the owl airfoil, the blade's maximum camber, maximum thickness, and their respective positions are altered, enhanced lift performance, increasing the maximum lift coefficient from 1.8 to 2.8 and raising the stall angle of attack from 12◦ to 14◦ (as shown in Figure 13a). While the drag coefficient is higher for low attack angles in the owl airfoil, resulting in increased drag, this is a necessary tradeoff for generating more lift (as shown in Figure 13b). However, as shown in Figure 13c, the owl airfoil consistently outperforms the conventional airfoil in terms of lift to drag ratio all angles of attack. There is a noticeable improvement in the lift-to-drag ratio when the angle of attack reaches 5 degrees. Between angles of 8 to 10 degrees, the aerodynamic performance remains relatively stable. However, beyond this range, in all sections, there appears to be a decline in performance, possibly attributed to an increase in drag.

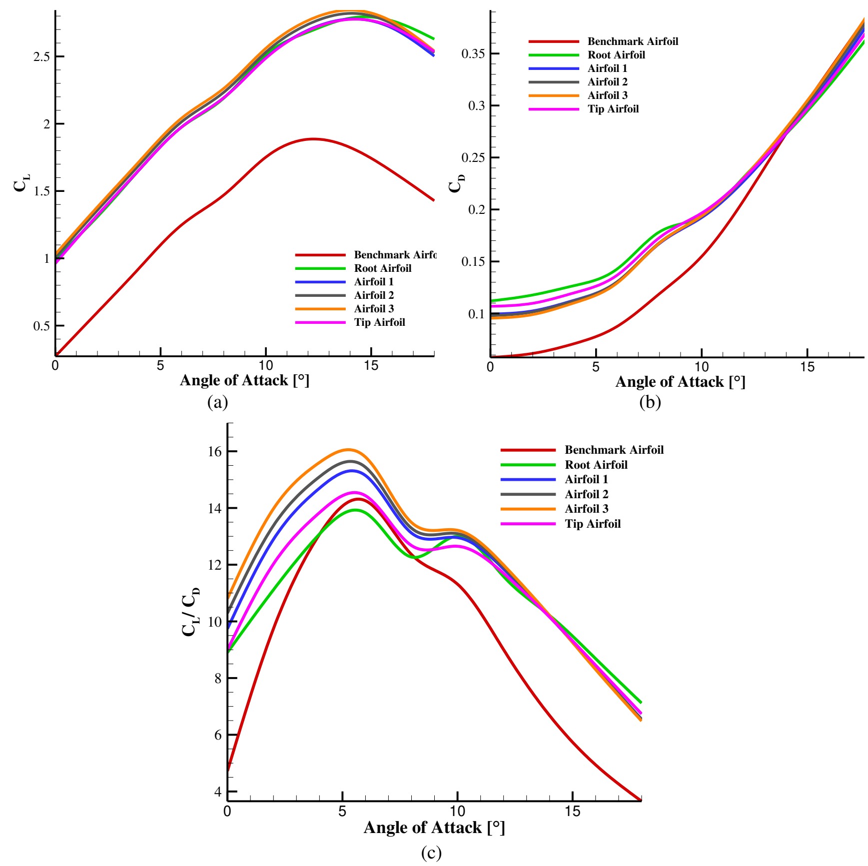

Figure 13: (a) Lift coefficients, (b) Drag coefficients and (c) Lift-to-drag ratio (Cl/Cd) curves of the airfoils at different AOA.

This section explores and presents the aerodynamic features of the turbine after the integration of the owl airfoil. The implementation of the owl airfoil on the turbine is carried out, and the resultant aerodynamic properties are studied and analyzed.

To better illustrate the changes in the flow field and interactions between the turbine and the boundary layer as a result of the inlet flow, a 2D section of the flow velocity is shown in the XY plane in Figure 14a. As can be seen, there are areas of low speed around the duct and turbine holder. At the same time, there are also high-speed areas at the ends of the blades and downstream (in the wake) which is 25 m/s. This indicates that the duct acts as a diffuser and increases the speed of the incoming air.

For Case 2, the instantaneous flow fields around the ducted wind turbine are shown using the Q criterion in Figure 14b. The figure illustrates the formation of vortices on the inner wall of the duct. Due to the increase in camber and changes in the thickness of the airfoil as the flow moves along the inner wall of the duct, the speed of the flow increases. The front vortices originate from the starting point of the inner side of the duct and adopt a helical shape as they get closer to the turbine. Consequently, this leads to an increase in turbulence structures and an increase in Turbulence Intensity (TI), which ultimately breaks up the larger front vortices into smaller ones. It also shows that the LES turbulence model predicts the turbulence fluctuations around a DWT well and provides a clearer picture of the complex flows around the turbine.

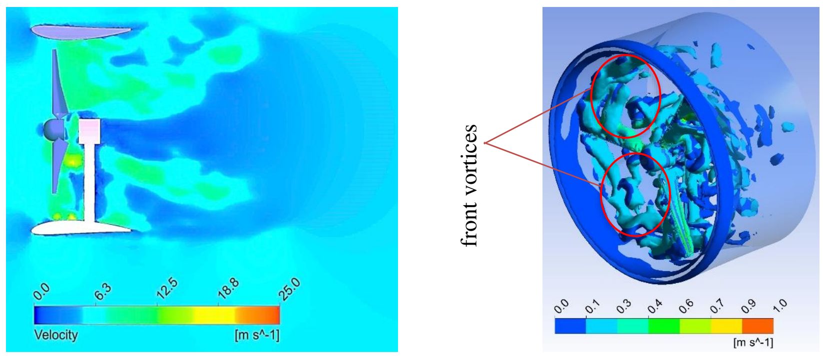

(a) (b)

Figure 14: (a) Velocity contour, (b) Q criterion.

In the context of a wind turbine, the conversion of mechanical energy into electrical energy hinges on the performance of the aerodynamic system, quantified as the power coefficient (C_{PWR}). In parallel, an essential factor in the design of turbine blades is the Tip Speed Ratio (TSR), representing the ratio between the linear speed of the blade tip and the wind speed. Consequently, this section delves into the variations in the power coefficient concerning TSR for both benchmark and multi-section blades. As illustrated in Figure 15, C_{PWR} exhibits a non-linear relationship with TSR, with the maximum C_{PWR} value occurring at TSR = 8 in both cases. This maximum value signifies the peak efficiency of the DWT. Thus, the selection of the optimal TSR value is of paramount importance. Furthermore, as depicted in the figure 15, for TSR values below 5, there is negligible discrepancy in C_{PWR} between the two blade types, with their performance differing by less than 10%. However, as TSR values increase, the C_{PWR} parameter demonstrates a significant rise, underscoring the benefit of employing multi-section blades.

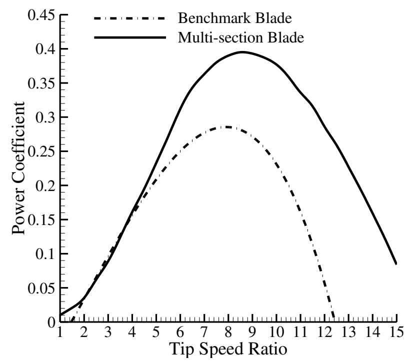

Figure 15: Variation in Power Coefficients for Benchmark and Multi-Section Blades across Various Tip Speed Ratio.

Aeroacoustics results

To investigate the sound around the turbine, according to Figure 16, thirty receivers are being used in the current study. The receivers are positioned at a distance of 1.5 times the chord length of the Duct airfoil. Receivers are spaced 12 degrees apart.

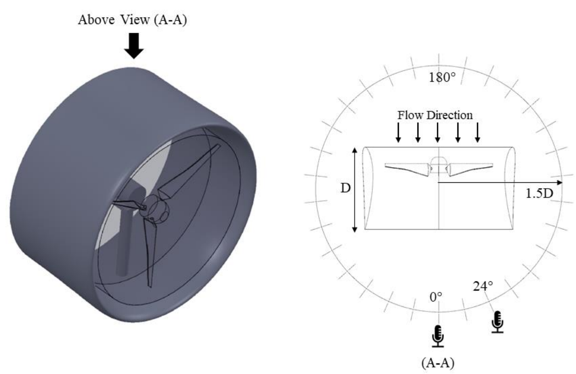

Figure 16: Receivers position.

Based on the receiver position curve, two specific points are analyzed in this study, point 1 at 0 degrees and point 2 at 24 degrees. Figure 17 displays sound pressure level graphs for both points, showing the frequency response for two cases. By implementing owl wing airfoils, noise generated by free stream turbulence and trailing edge noise is reduced. Notably, this improvement has the most significant impact on higher frequencies. The multi-section results suggest that owl-inspired airfoils have proven effective in mitigating noise.

According to the polar curve of Overall Sound Pressure Level (OASPL), as shown in Figure 18 based on the position of the receivers, it can be seen that the use of airfoils of owl-inspired reduces the sound by an average of 6-8 decibels at 60 to -60 degrees (which represents the flow exit area from the duct). As can be seen, in some positions, including 90 and 270 degrees, there is no change in the OASPL curve for owl-shaped wing (multi-section blade). It does not reduce sound in the radial direction. As a result, to reduce sound, it is recommended to make changes such as using perforated plates in the structure of the duct and its surfaces, as well as adding sound-absorbing materials inside.

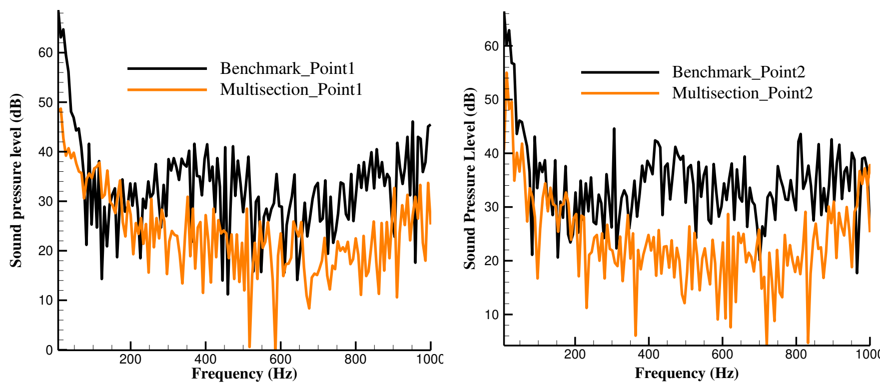

(a) (b)

Figure 17: Comparison between SPL vs Frequency of 2 cases study at point1 (a) and point2 (b).

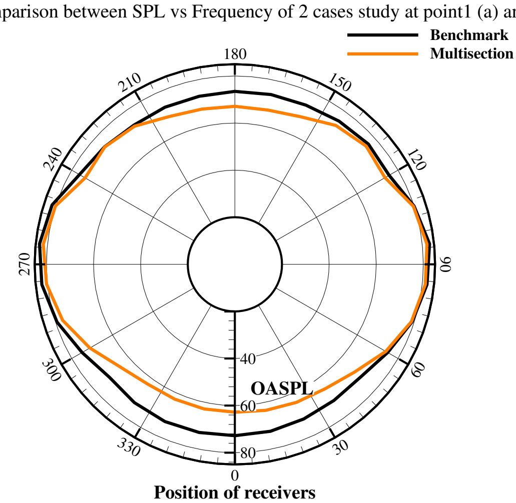

Figure 18: Comparison between SPL of 2 cases study around the ducted.

As can be seen in Figure 19a, the highest sound pressure level occurs on the inner surface of the duct which the lowest level is on the outer surfaces of the duct. The highest SPL value on the inner surface of the duct is typically associated with the airfoil's thickest portion located at the leading edge. As a result, the use of a duct as a diffuser cover significantly reduces the sound and act as a barrier, as well as protect the surrounding environment from damage. Based on the contour presented in figure 19b, it appears that altering the blade foils did not result in any detrimental impact on the level of noise produced at the tip of the turbine duct. Also, figures 19 illustrates how the surface under the airfoil, which is the suction area, has a more significant effect on noise production. An explanation for this can be found in the change in the camber line and the changes in the thickness of the airfoil. Therefore, it leads to an increase in turbulence structures and pressure fluctuations, resulting in more sound being produced on the lower surface of the airfoil. With comparing Figures 19a and 19b, it becomes apparent that the SPL value has decreased both downstream and on the inner surface of the duct. Further analysis can be conducted by referring to Figure 19c, which illustrates sound pressure levels specifically along the inner surface of the duct. In this segment, a section is formed on the interior of the duct. It is worth noting that modifications made to the turbine blade have a noticeable effect on the noise generated downstream, leading to a reduction in noise at the trailing edge of the inner duct. This noise reduction is approximately equal to 10 dB in all positions after the turbine tower. Intriguingly, the use of multi-section blades does not impact the noise levels in front of the rotor.

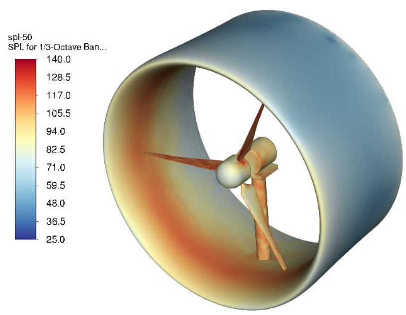

(a)

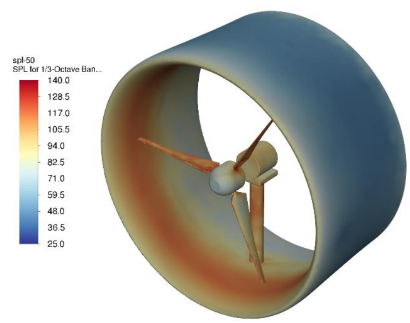

(b)

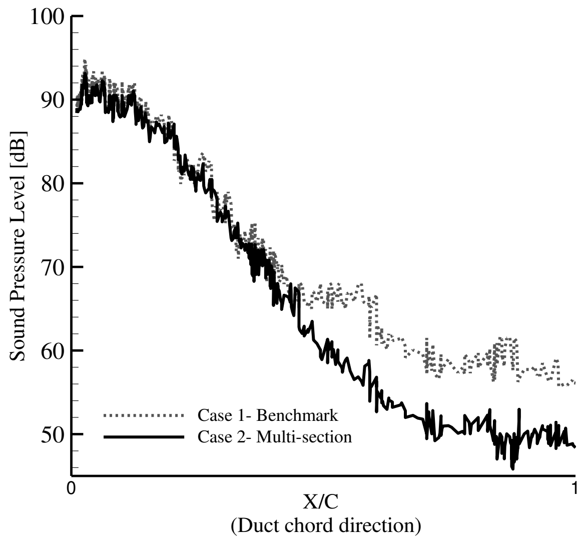

(c)

Figure 19: Noise level contour for frequency 50 Hz for cases number 1 (a) and 2 (b) and (c) Comparative Analysis of Sound Pressure Levels along the Inner Duct Surface between Cases 1 and 2.

Upon analyzing the frequencies ranging from 50 Hz to 500 Hz in case number 2 as shown in Figure 20, it becomes apparent that noise levels decrease as the frequency increases. The maximum noise production within the duct occurs in the regions near the leading edge to the tower, with the highest levels of noise generated in the corresponding areas of the blade tips. Also, this figure indicates that the most effective place to reduce noise is this area, which is the logical point to consider the perforated plate (punch) along with the absorber at the position of the inner junction to the turbine tower to the duct.

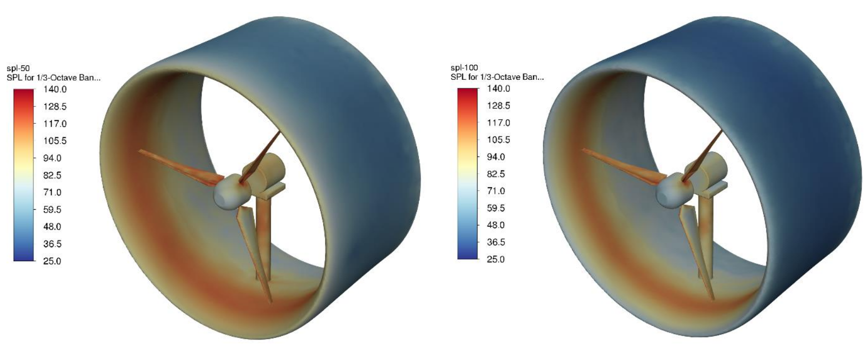

(a) 50 Hz (b) 100 Hz

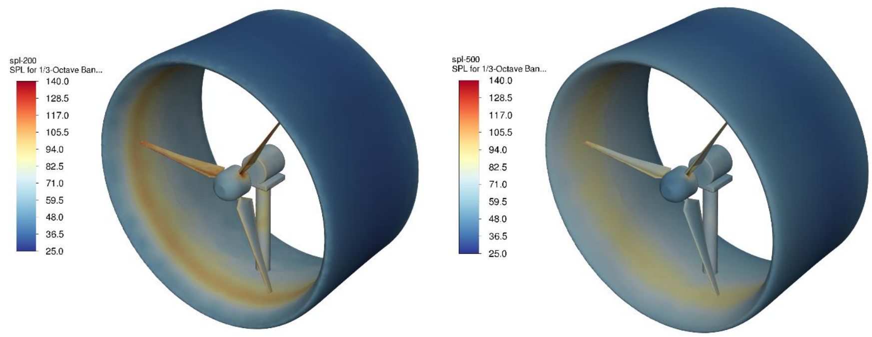

(c) 200 Hz (d) 500 Hz

Figure 20: Noise level contour for frequencies 50 Hz to 500 Hz for case number 2.

Conclusions

In this comprehensive study, we have employed advanced Large Eddy Simulation (LES) turbulence modeling and Ffowcs Williams-Hawkings (FW-H) acoustic analogy to meticulously analyze the aeroacoustic and aerodynamic properties of ducted wind turbine blades. These blades are innovatively designed, drawing inspiration from the silent flight mechanism of owl wings. Our primary aim was to address the critical challenge of reducing aerodynamic noise, particularly the noise generated by inflow turbulence and trailing edges, while concurrently ensuring that the aerodynamic performance remains uncompromised.

The investigation revealed that the incorporation of bio-inspired airfoil sections, meticulously derived from owl wings through 3D scanning techniques, significantly influences the noise reduction and aerodynamic efficiency of wind turbines. Specifically, the application of these uniquely designed airfoils resulted in a notable reduction of aerodynamic noise by approximately 8 decibels, which translates to an improvement of about 12% when compared to conventional designs. This achievement underscores the potential of bio-inspired modifications in enhancing the environmental compatibility of wind turbines, particularly in urban settings where noise pollution is a significant concern.

Moreover, our results demonstrated a 6.4% increase in the thrust force coefficient for the multi-section blade compared to the conventional blade design. The power coefficient analysis further revealed that the maximum power coefficient occurred at a Tip Speed Ratio (TSR) of 8 for both the benchmark and multi-section blades, emphasizing the optimized aerodynamic efficiency achieved through the bio-inspired design.

Furthermore, our study delved into the aeroacoustic performance, where the findings indicated a substantial noise reduction in specific areas around the duct, especially downstream and on the inner surface. These results suggest that the strategic implementation of owl-inspired airfoil profiles not only benefits the noise profile but also contributes to the overall aerodynamic efficiency of the turbine. However, it's worth noting that the radial sound suppression remained unaffected, suggesting additional avenues for enhancing the aeroacoustic performance, possibly through further structural modifications or the integration of sound-absorbing materials.

In conclusion, this research not only contributes valuable insights into the aeroacoustic and aerodynamic optimization of wind turbines but also highlights the potential of bio-inspired designs in the field of renewable energy. The significant reduction in noise levels, coupled with the maintenance of aerodynamic performance, presents a compelling case for the adoption of such innovative design strategies in future wind turbine development, particularly in noise-sensitive environments. Our findings lay a solid foundation for future studies and the practical application of bio-inspired designs in enhancing the sustainability and community acceptance of wind energy solutions.

Data Availability

The data used to support the findings of this study are available from the corresponding author upon request.

Conflicts of Interest

The authors declare that there is no conflict of interest regarding the publication of this paper.

Funding Statement

The authors have no relevant financial or non-financial interests to disclose.

Acknowledgments

Our research would not have been possible without the support of Iran Wildlife and Nature Museum - Dar Abad and Huber 3D scan engineering group, who provided us with a great deal of assistance.

References

[1] A.H. Butt, B. Akbar, J. Aslam, N. Akram, M.E.M. Soudagar, F.P.G. Márquez, M.Y. Younis, E. Uddin, "Development of a linear acoustic array for aero-acoustic quantification of camber-bladed vertical axis wind turbine," Sensors (Switzerland), vol. 20, pp. 1-17, 2020.

[2] M. Ilie, J.W. McAfee, "Aerodynamics and design of vertical-axis wind turbine; numerical studies using les and iddes," in AIAA AVIATION 2020 FORUM, 2020, pp. 1-9.

[3] T. Fukano, C.-M. Jang, "Tip clearance noise of axial flow fans operating at design and off-design condition," Journal of sound and vibration, vol. 275, pp. 1027-1050, 2004.

[4] H. Weger, M. Weger, M. Klaas, W. Schröder, "Features of owl wings that promote silent flight," Interface Focus, vol. 7, 2017.

[5] R. Graham, "The silent flight of owls," The Aeronautical Journal, vol. 38, pp. 837-843, 1934.

[6] E. Mascha, "Über die schwungfedern," Zeitschrift für wissenschaftliche Zoologie, vol. 77, pp. 606-651, 1904.

[7] L. Wang, X. Liu, D. Li, "Noise reduction mechanism of airfoils with leading-edge serrations and surface ridges inspired by owl wings," Physics of Fluids, vol. 33, 2021.

[8] R. Hayden, "Reduction of noise from airfoils and propulsive lift systems using variable impedance systems," in 3rd AIAA Aeroacoustics Conf., Palo Alto, CA, USA, 1976.

[9] P. Chaitanya, P. Joseph, S. Narayanan, C. Vanderwel, J. Turner, J.-W. Kim, B. Ganapathisubramani, "Performance and mechanism of sinusoidal leading edge serrations for the reduction of turbulence–aerofoil interaction noise," Journal of Fluid Mechanics, vol. 818, pp. 435-464, 2017.

[10] B.Y. Zhou, S.R. Koh, N.R. Gauger, M. Meinke, W. Schöder, "A discrete adjoint framework for trailing-edge noise minimization via porous material," Computers & Fluids, vol. 172, pp. 97-108, 2018.

[11] C. Pimenta, W.R. Wolf, A.V. Cavalieri, "A fast numerical framework to compute acoustic scattering by poroelastic plates of arbitrary geometry," Journal of Computational Physics, vol. 373, pp. 763-783, 2018.

[12] J.M. Turner, J.W. Kim, "Aeroacoustic source mechanisms of a wavy leading edge undergoing vortical disturbances," Journal of Fluid mechanics, vol. 811, pp. 582-611, 2017.

[13] E. Sarradj, C. Fritzsche, T. Geyer, "Silent owl flight: Bird flyover noise measurements," AIAA journal, vol. 49, pp. 769-779, 2011.

[14] K. Lee, Y. Kozato, S. Kikuchi, S. Imao, "Numerical simulation of flow control around a rectangular cylinder by dielectric barrier discharge plasma actuators," Physics of Fluids, vol. 34, 2022.

[15] E. Fatahian, F. Ismail, M.H.H. Ishak, W.S. Chang, "Aerodynamic performance improvement of savonius wind turbine through a passive flow control method using grooved surfaces on a deflector," Ocean Engineering, vol. 284, p. 115282, 2023.
[16] F. Eydi, A. Mojra, R. Abdi, "Comparative analysis of the flow control over a circular cylinder with detached flexible and rigid splitter plates," Physics of Fluids, vol. 34, 2022.
[17] W. Song, Z. Mu, Y. Wang, Z. Zhang, S. Zhang, Z. Wang, B. Li, J. Zhang, S. Niu, Z. Han, "Comparative investigation on improved aerodynamic and acoustic performance of abnormal rotors by bionic edge design and rational material selection," Polymers, vol. 14, p. 2552, 2022.
[18] T. Liu, K. Kuykendoll, R. Rhew, S. Jones, "Avian wing geometry and kinematics," AIAA journal, vol. 44, pp. 954-963, 2006.
[19] S. Klań, T. Bachmann, M. Klaas, H. Wagner, W. Schröder, "Experimental analysis of the flow field over a novel owl based airfoil," Animal Locomotion, pp. 413-427, 2010.
[20] T. Bachmann, G. Mühlenbruch, H. Wagner, "The barn owl wing: An inspiration for silent flight in the aviation industry?," in Bioinspiration, Biomimetics, and Bioreplication, 2011, pp. 142-155.
[21] T. Geyer, E. Sarradj, C. Fritzsche, "Silent owl flight: Acoustic wind tunnel measurements on prepared wings," in 18th AIAA/CEAS Aeroacoustics Conference (33rd AIAA Aeroacoustics Conference), 2012, p. 2230.
[22] K. Kondo, H. Aono, T. Nonomura, M. Anyoji, A. Oyama, T. Liu, K. Fujii, M. Yamamoto, "Analysis of owl-like airfoil aerodynamics at low reynolds number flow," Transactions of the Japan Society for Aeronautical and Space Sciences, Aerospace Technology Japan, vol. 12, pp. Tk_35-Tk_40, 2014.
[23] W. Tian, Z. Yang, Q. Zhang, J. Wang, M. Li, Y. Ma, Q. Cong, "Bionic design of wind turbine blade based on long-eared owl's airfoil," Applied Bionics and Biomechanics, vol. 2017, 2017.
[24] M. Anyoji, S. Wakui, D. Hamada, H. Aono, "Experimental study of owl-like airfoil aerodynamics at low reynolds numbers," Journal of Flow Control, Measurement & Visualization, vol. 6, p. 185, 2018.
[25] F. Moslem, M. Masdari, K. Fedir, B. Moslem, "Experimental investigation into the aerodynamic and aeroacoustic performance of bioinspired small-scale propeller planforms," Proceedings of the Institution of Mechanical Engineers, Part G: Journal of Aerospace Engineering, vol. 237, pp. 75-90, 2023.
[26] H. Aono, K. Kondo, T. Nonomura, M. Anyoji, A. Oyama, K. Fujii, M. Yamamoto, "Aerodynamics of owl-like wing model at low reynolds numbers," Transactions of the Japan Society for Aeronautical and Space Sciences, vol. 63, pp. 8-17, 2020.
[27] M. Muthuramalingam, E. Talboys, H. Wagner, C. Bruecker, "Flow turning effect and laminar control by the 3d curvature of leading edge serrations from owl wing," Bioinspiration & Biomimetics, vol. 16, p. 026010, 2020.
[28] N. Ricks, P. Tsirikoglou, F. Contino, G. Ghorbaniasl, "A cfd-based methodology for aerodynamic-aeroacoustic shape optimization of airfoils," in AIAA Scitech 2020 Forum, 2020, p. 1729.
[29] H. Gruschka, I. Borchers, J. Coble, "Aerodynamic noise produced by a gliding owl," Nature, vol. 233, pp. 409-411, 1971.
[30] T. Wolf, R. Konrath, "Avian wing geometry and kinematics of a free-flying barn owl in flapping flight," Experiments in Fluids, vol. 56, pp. 1-18, 2015.
[31] V.V. Dighe, F. Avallone, G. van Bussel, "Effects of yawed inflow on the aerodynamic and aeroacoustic performance of ducted wind turbines," Journal of Wind Engineering and Industrial Aerodynamics, vol. 201, 2020.
[32] K. Güzey, U.E. Aylı, E. Kocak, S. Aradag, "Investigation of aerodynamic and aeroacoustic behavior of bio-inspired airfoils with numerical and experimental methods," Proceedings of the Institution of Mechanical Engineers, Part C: Journal of Mechanical Engineering Science, p. 09544062231185495, 2023.
[33] F. Eydi, A. Mojra, "A numerical study on the benefits of passive-arc plates on drag and noise reductions of a cylinder in turbulent flow," Physics of Fluids, vol. 35, 2023.
[34] Y. Wang, T. Mikkola, S. Hirdaris, "A fast and storage-saving method for direct volumetric integration of fwh acoustic analogy," Ocean Engineering, vol. 261, p. 112087, 2022.
[35] D. Romik, I. Czajka, "Numerical investigation of the sensitivity of the acoustic power level to changes in selected design parameters of an axial fan," Energies, vol. 15, p. 1357, 2022.
[36] S. Gant, "Practical quality measures for large-eddy simulation," in Direct and Large-Eddy Simulation VII: Proceedings of the Seventh International ERCOFTAC Workshop on Direct and Large-Eddy Simulation, held at the University of Trieste, September 8-10, 2008, 2010, pp. 217-222.
[37] T. Hoopen, "An experimental and computational investigation of a diffuser augmented wind turbine: With an application of vortex generators on the diffuser trailing edge," Ph.D. thesis, Delft University of Technology, Delft, The Netherlands, 2009.